

1 **A processing pipeline for image reconstructed fNIRS analysis using both MRI templates and**
2 **individual anatomy**

3
4 **Samuel H. Forbes,^a Sobanawartiny Wijekumar,^b Adam T. Eggebrecht,^c Vincent A.**
5 **Magnotta,^d John P. Spencer^{a,*}**

6 ^aUniversity of East Anglia, School of Psychology, Lawrence Stenhouse Building, Norwich, UK,
7 NR4 7TJ

8 ^bUniversity of Nottingham, School of Psychology, University Park, Nottingham, UK, NG7 2RD

9 ^cWashington University, Mallinckrodt Institute of Radiology, 4515 McKinley Ave, St Louis, MO,
10 USA, 63110

11 ^dUniversity of Iowa, Department of Radiology, 200 Hawkins Drive, Iowa City, IA, USA, 52242

12

13 **Abstract. Significance:** Image reconstruction of fNIRS data is a useful technique for transforming
14 channel-based fNIRS into a volumetric representation and managing spatial variance based on
15 optode location. We present a novel integrated pipeline for image reconstruction of fNIRS data
16 using either MRI templates or individual anatomy.

17 **Aim:** We demonstrate a pipeline with accompanying code to allow users to clean and prepare
18 optode location information, prepare and standardize individual anatomical images, create the light
19 model, run the 3D image reconstruction, and analyze data in group space.

20 **Approach:** We synthesize a combination of new and existing software packages to create a
21 complete pipeline, from raw data to analysis.

1 **Results:** This pipeline has been tested using both templates and individual anatomy, and on data
2 from different fNIRS data collection systems. We show high temporal correlations between
3 channel-based and image-based fNIRS data. In addition, we demonstrate the reliability of this
4 pipeline with a sample dataset that included 74 children as part of a longitudinal study taking place
5 in Scotland. We demonstrate good correspondence between data in channel space and image
6 reconstructed data.

7 **Conclusions:** The pipeline presented here makes a unique contribution by integrating multiple
8 tools to assemble a complete pipeline for image reconstruction in fNIRS. We highlight further
9 issues that may be of interest to future software developers in the field.

10 **Keywords:** fNIRS, DOT, Image Reconstruction, Individual Anatomy

11

12 *JPS, E-mail: j.spencer@uea.ac.uk

13

14 **1 Introduction**

15 In recent years there has been a rise in the usage of functional Near Infra-Red Spectroscopy
16 (fNIRS) in neuroimaging studies (1–5). fNIRS is a safe, non-invasive method of neuroimaging,
17 which measures the concentration of oxygenated and deoxygenated hemoglobin. fNIRS has
18 become an important neuroimaging tool for developmental neuroscience and other fields where
19 participant characteristics, naturalistic study paradigms, or costs make functional MRI difficult to
20 use, such as in low-resource settings (6–8).

21 A key limitation of fNIRS is that optode locations can vary, making it difficult to compare
22 across participants within a study as well as across studies. Spatial variance in brain sampling can

1 occur due to slight differences in cap placement on the head. But even with precise cap placement,
2 variance can occur due to subtle differences in head shape and size. This makes it challenging to
3 make robust inferences across participants from analyses conducted in channel space given
4 potentially erroneous but strong assumptions about the consistent placement of source-detector
5 pairs relative to functional brain areas.

6 To overcome this limitation, there have been key innovations in image-reconstructed fNIRS
7 which uses a head model as a spatial prior to transform channel-based fNIRS data into a volumetric
8 representation. Such approaches use either Monte Carlo simulations of photon migration in the
9 brain (9), or solve the photon diffusion equation (10), to move statistical analyses from channel
10 space on the surface of the head into voxel space within the brain volume. Using such methods,
11 therefore, localizes patterns of activation from fNIRS into specific brain regions, allowing for more
12 robust comparisons across participants and groups as data are registered into a common space. In
13 image-reconstruction approaches, the head model used for reconstruction typically comes from an
14 anatomical head atlas (1,11–14), although one can also use subject-specific anatomy from an
15 individual MRI scan (15).

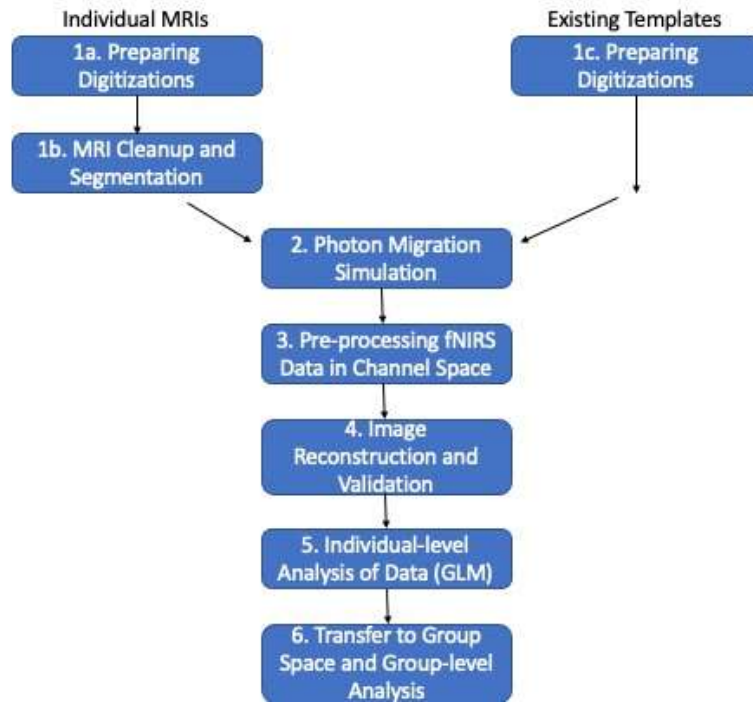
16 To date, the majority of image-reconstruction approaches have used anatomical templates,
17 where a template atlas is used for registering the digitization and transforming into subject space.
18 While this allows for uniformity and consistency between subjects, it overlooks the role that
19 individual anatomical differences may play in the analyses. A subject with higher-than-average
20 CSF in a particular area of the brain, for example, will have different tissue properties in that region
21 which will lead to different amounts of scattering and absorption of near infra-red light. The use
22 of individual anatomy allows such individual-level differences to inform the analyses. However,

1 standardizing and preparing individual anatomies adds layers of complexity to the analysis -- a
2 hurdle which is addressed in the present article.

3 The process of image reconstruction, particularly when using subject-specific anatomy is
4 complex and requires multiple steps. Optode locations must be collected and checked relative to a
5 template, with a method for correcting any digitization errors. The digitized positions must then
6 be formatted for use with software that can create a light model. Individual MRI images must be
7 optimized through removal of background noise, and the image must then be segmented to create
8 the tissue model needed for photon migration simulations. The segmented head and optode
9 locations then need to be aligned and photon migration simulations run to create the sensitivity
10 profiles needed for image reconstruction. The fNIRS data then needs to be pre-processed in
11 channel space and combined with the sensitivity profiles for image reconstruction. These subject-
12 specific results then need to be analyzed at the individual level (e.g., using a general linear
13 modelling approach) and aligned in a common group space for statistical analysis.

14 A current difficulty for this type of work is the lack of analysis pipelines that pull all of these
15 steps together. No current software or published pipeline covers all aspects of this approach,
16 making it difficult for users to have an integrated approach that includes image reconstruction
17 within the full scope of the processing pipeline. The present article, therefore, presents a pipeline
18 that takes the user from the initial pre-processing and cleanup steps all the way through to group
19 analysis, with the hope that this will lead to greater transparency of results and make data sharing
20 easier between research groups. The tools employed in this pipeline are all publicly available
21 online.

1 1.1 Overview of the Pipeline



2
3 *Figure 1. A flow diagram demonstrating the use of this pipeline. Steps on the left indicate steps*
4 *to be taken with individual MRI images, steps on the right indicate steps to be taken using an*
5 *existing template image.*

6
7 Figure 1 shows the steps to be followed using this pipeline. These steps are detailed below.

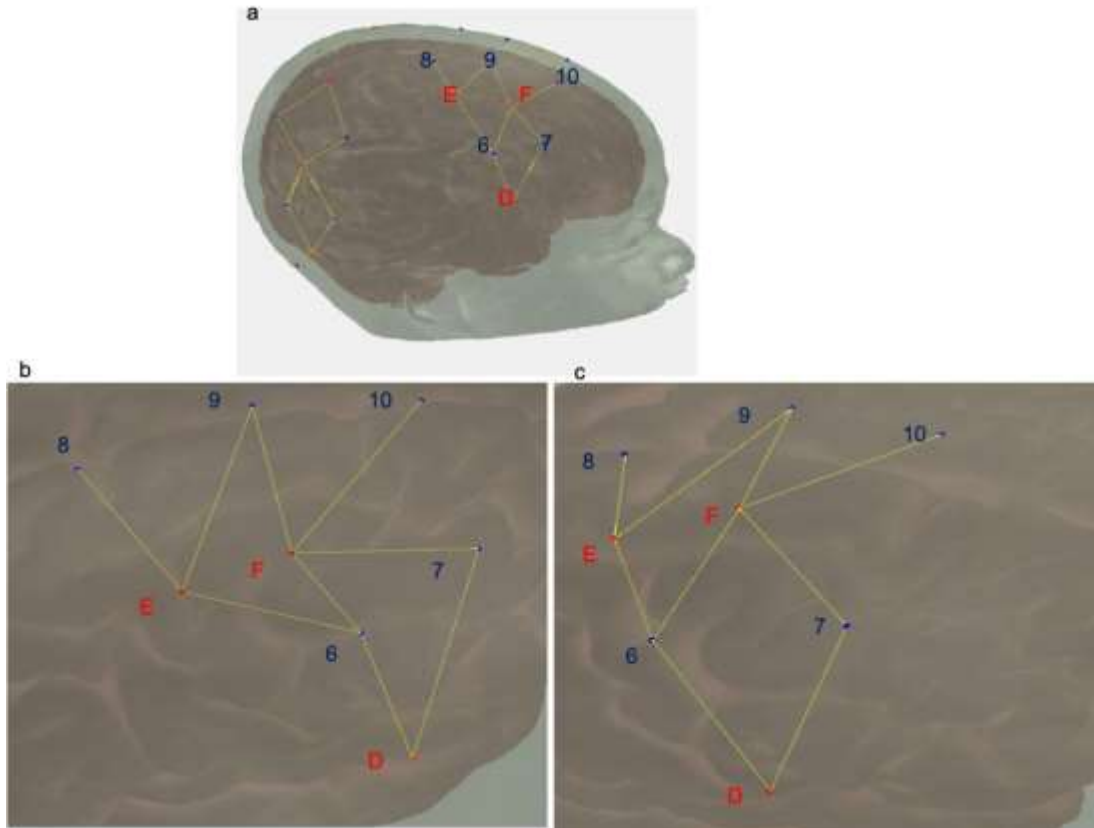
8 Briefly, the first step handles preparing and cleaning the digitization data, that is, estimates of the
9 3D positions of the fNIRS optodes on the head. Next, we discuss how to prepare the MRI
10 images. Here we focus on preparing individual MRI images (see left, top in Figure 1). For
11 studies using an atlas that already contains a segmented head (see right, top in Figure 1), the user
12 can skip to setting up and running Monte Carlo simulations to create the light model. Where
13 users have a template MRI which has not yet been segmented, they may wish to use the
14 segmentation steps described in this pipeline, but bypassing the cleaning steps, similar to a user
15 in possession of individual MRIs without background noise in a good orientation. Nonetheless it
16 is recommended that users read the steps on preparing individual anatomical files to determine
17 whether their files meet the formatting requirements.

1 Once the MRI data are prepared, the next step is to create the light model. There are
2 multiple software packages that handle this step; we describe one implementation using Homer2
3 (<https://homer-fnirs.org/>) (16). Note that the pipeline is also fully compatible with Homer3 as
4 well. Then, fNIRS data must be pre-processed. Again, there are multiple options here, and we
5 describe a solution using Homer2. The next step is image reconstruction. Here, we use tools from
6 the NeuroDOT package (17) (https://github.com/WUSTL-ORL/NeuroDOT_Beta). We then run
7 an individual-level GLM on the data, again, using NeuroDOT tools. Finally, we describe how to
8 transfer the data into a common group space for a group-level analysis. We demonstrate the final
9 data produced by the pipeline using recent data from a study looking at the development of
10 visual working memory in children. All code and full documentation for the pipeline steps can be
11 found on the github sites described in each section below.

12 **2 Preparing Digitizations**

13 *2.1 Collecting digitization data*

14 To locate the optodes on the head, we collect digitizations with a Polhemus Patriot FCC Class B
15 digitizing device (<https://polhemus.com/scanning-digitizing/digitizing-products/>). The device
16 consists of an electromagnetic receiver, placed on top of the head, and a wand used to mark the
17 placement of the tip at each optode. The device default is set to capture the locations in inches
18 from the receiver, but we changed this to centimeters to be compatible with Homer2 (14,16) (which
19 we use in subsequent pipeline steps). Typically, digitizations are assumed to be in the format of
20 one point per row, where the first set of points are reference landmarks on the head, followed by
21 the sources, and then the detectors. Figure 2 shows a typical digitization captured with a small
22 amount of error, pulling points out of alignment (in this case due to reaching across the head).



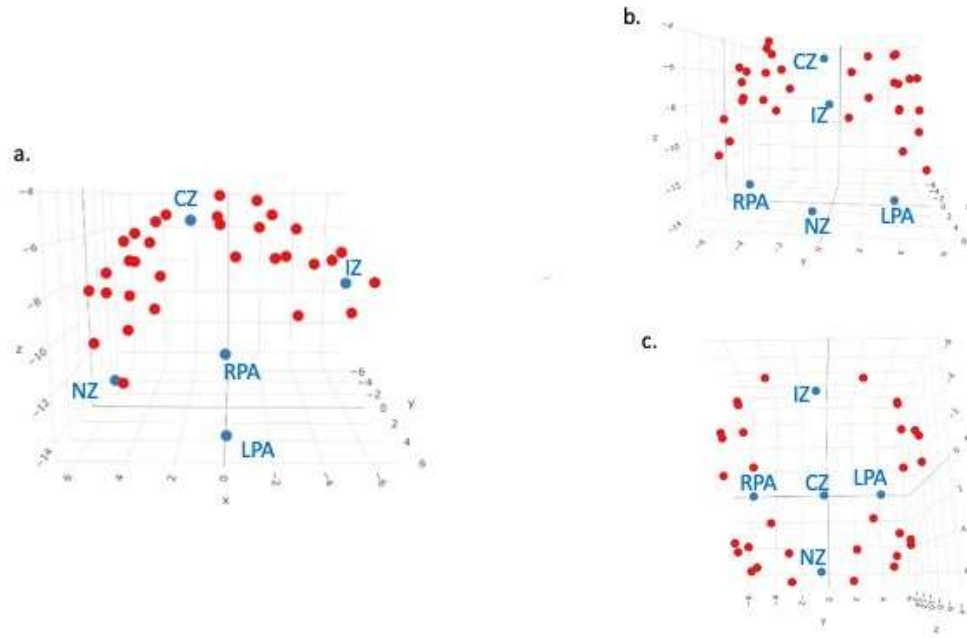
1
 2 *Figure 2.* (a) The full cap layout. (b) A standard digitization with some error on the part of the
 3 experimenter, where the area shown is the highlighted region of (a). Detectors 6 and 7 (blue) have
 4 been digitized out of alignment with sources D, E, and F (red). c. The same digitization following
 5 3-point correction. Note that the layout in (c) is the expected layout, matching the highlighted
 6 region in (a).

7 *2.2 Creating digitization templates*

8 One of the challenges of using a digitizing pen is that errors in positioning can arise. For instance,
 9 in Figure 2, several points are slightly mis-localized resulting in a distorted geometry. This can be
 10 caused by a slight slippage in the digitizing pen when the participant moves, inducing a slight mis-
 11 localization of the pen tip. Such minor errors are difficult to identify on the fly, particularly when
 12 the head being digitized is on the body of a squirmy child. To combat errors in mis-localization

1 of points, we developed a package for the R language (<https://www.r-project.org/>), *digitizeR*
2 (www.github.com/samhforbes/digitizeR), which takes digitized input from multiple participants
3 for a given head size, creates a digitization template, and identifies and fixes mis-localization errors
4 in individual caps.

5 In particular, once collected, the digitizations for each participant can be read into *digitizeR*
6 by cap size. For ease of visualizing caps as they change, we also recommend RStudio. The
7 *digitizeR* package will read in the Polhemus output files (saved in ASCII text format) and create a
8 list for each cap size. Next, *digitizeR* finds the best caps to align the other caps to for each cap size.
9 This is done using the Kabsch algorithm (18), a method of finding the optimal rotation between
10 two matrices to reduce the root mean squared deviation. *DigitizeR* uses this algorithm to align each
11 cap to all the other caps in that size. Since every digitization runs the risk of participant movement
12 throwing off the values for any given point (or the entire cap), each cap is rotated to match every
13 other cap. The assumption here is that all the caps that were digitized well will all align with each
14 other, and the caps that were digitized poorly will fail to align. So, for example, for three caps A,
15 B, and C, if caps A and B are good caps, and C is a poor digitization, A will align with B within a
16 given 3D criterion distance and B will align with A, whereas C will align with neither A nor B.
17 The next step is to use this information about which caps align to create a template. In our
18 hypothetical situation, two caps, A and B, align with each other within the criterion distance, so
19 the template will be defined by calculating the 3D mean of each corresponding point in A and B.
20 Using this process, a template cap is created for each cap size.



1
 2 *Figure 3.* A 3D image of a template created from a group of caps, from digitizeR. Points in blue
 3 are head landmarks, points in red are digitized points from the fNIRS cap. Landmarks have been
 4 labelled. (a) shows the cap from the left-hand side, (b) from the front, and (c) from the top.

5
 6 Figure 3 shows a template created from a group of caps. In this instance, the template
 7 digitization was created from a group of caps with a head circumference of 48cm. Caps were
 8 aligned using the above method where the 3D distance threshold was chosen as 10cm. This took
 9 the reference cap with the most other matches at that cap size where no point was allowed to exceed
 10 a 3D distance of 10cm from the reference; in this instance the aligned caps had a mean distance of
 11 3.91cm from the reference cap. The mean of each of the points across all of the matching caps was
 12 then calculated to create the template.

13 Once created, templates can be saved in digitizeR and used for all participants in that cap
 14 size if desired. This would yield an average acceptable digitization that is unique to each cap size,

1 but captures the data collected across the sample. Alternatively, as we describe in the next section,
2 digitizeR allows using the template to clean and save modified versions of the individual
3 digitizations, allowing the user to preserve as much of the individual-level variation in optode
4 location and cap placement as possible.

5 *2.3 Correcting individual caps*

6 Once templates have been constructed, each participant cap can then be aligned to the template for
7 that cap size, again using the Kabsch algorithm. There are two sources of variation in the digitized
8 locations in 3D space: true variation in cap placement and optode location due to factors such as
9 wrinkles in the cap or the cap being off-center; and errors such as digitization of the incorrect point
10 or movement causing the point to be unrealistically far away from the head. The goal of the
11 correction at the individual cap level is to permit as much of the former variance as possible, which
12 is due to the true placement of the optode on the head, while eliminating the large sources of the
13 latter type of variance.

14 The digitizeR package allows three different correction methods: a three-step alignment
15 correction method, an iterative method, and a head-wise method. The three-step method allows
16 the user to specify three threshold 3D distances, at which the points will be sequentially tested
17 against the template for that cap size, and those outside those distances will be removed, and then
18 the cap re-aligned without those points. As an example, a 3-step alignment on a digitization with
19 distances set at 12, 8, and 6 would first exclude points beyond a 3D distance of 12(cm), re-align
20 without those points and do a second pass with a threshold of 8cm, re-align without those points
21 and then do a third pass with a threshold of 6cm, removing the points beyond this threshold. After
22 the final distance check, the missing points are replaced with points from the relevant template.
23 The difficulty with the three-step method is selecting the three distances, and this can be dependent

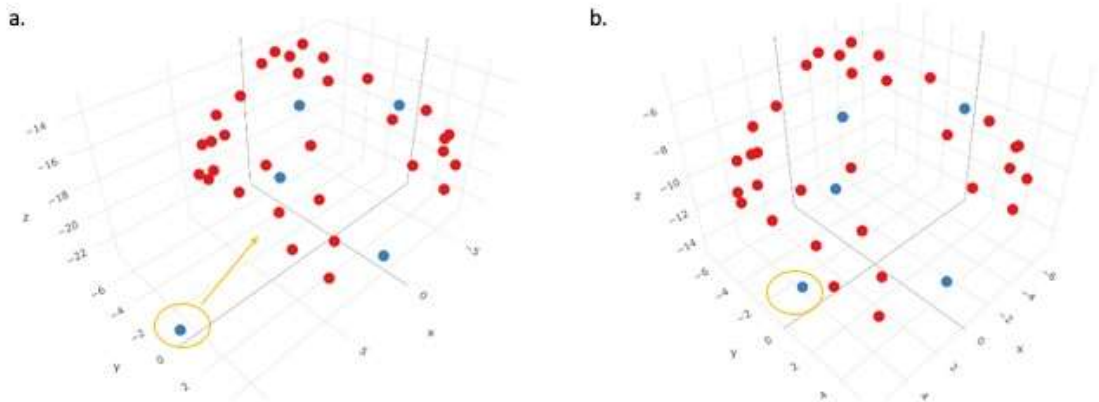
1 on the data that is being used. The data that were cleaned using the template in Figure 3 were
2 cleaned using threshold distances of 12, 10 and 7cm, with the end goal of making sure no more
3 than 1/3 of the original data points had been replaced using this method.

4 The iterative approach takes the same method as the three-step approach, but rather than the
5 user-specified distances, it starts with a 3d distance of 20cm and replaces points outside of that
6 distance, and then reduces the difference by 1cm, repeating the procedure of aligning to the
7 template and removing the points outside of the 3D distance each time until the points replaced
8 reach the user-specified proportion of replaced points, or until the points are within half a
9 centimeter of the template. The headwise method follows a similar logic, but deals with entire caps
10 rather than individual points, so that rather than individual points being replaced, the mean 3D
11 distance from all the points in the cap is calculated against the template, and caps exceeding the
12 threshold distance are replaced with a complete template cap, otherwise the cap remains as it was.

13 In this report, we used the three-step method which uses the R function
14 `threestep_alignment()`, although the best approach may be dependent on the types of errors being
15 seen in the data. In the case of our dataset, we wanted to minimize the number of points we were
16 replacing while ensuring our caps were as correct as possible. While some trial and error can be
17 necessary to determine the best distances for the caps at hand, the three-point method is a good
18 option for this purpose. The points that were removed as part of this procedure are then filled in
19 with the equivalent point from the template once the cap is aligned to make a complete cap that is
20 aligned in the same space as the template cap.

21 We tested the three-step method by taking two templates, loading them in as caps, and
22 moving the first point (the landmark NZ) much further away from the other points. We then used
23 the original templates to repair them. The test of this method is that the three-step alignment

1 correction should correct that point on each of the two templates, but no other points, as all other
2 points derive from the template itself. When this is tested with the three-step method, only these
3 two bad points are corrected, having been replaced with the original template points, and all other
4 points remain the same.



5
6 *Figure 4.* A demonstration of the validation of the three-step alignment correction. The
7 circled point in (a) is the one that was moved out from the template, and in (b) this point is back
8 in place, while the rest of the points remain unaffected.

9 *2.4 Preparing for use with Homer2/ Homer3*

10 The final versions of the digitized caps after alignment to the template can be saved and exported
11 from R using the built-in functions from the digitizeR package. The save_caps option
12 automatically saves each of the caps in its own folder as a digpts.txt file, saved in the format that
13 is necessary for Homer2/Homer 3, which includes reference, source, or detector labels for each
14 point. In addition, the caps are converted by default to distances in millimeters (from centimeters),

1 making them automatically ready to use for import into Homer2 or Homer3. Full documentation
2 for any of the digitizeR functions can be found at www.github.com/samhforbes/digitizeR.

3 **3 MRI Cleanup and Segmentation**

4 One of the challenges with fNIRS image reconstruction currently is that there are few pipelines
5 that can handle both atlas-based and individual-MRI-based registration. The latter case is
6 particularly challenging as individual MRIs require both cleanup and segmentation before this
7 information can be used in the registration process. These steps can be quite challenging,
8 particularly in developmental research as infant and child MRI data can have unique
9 characteristics. Thus, in this section, we describe steps in our pipeline to help researchers
10 standardize MRI cleanup and segmentation.

11 The segmentation process is based on having an anatomical T1-weighted image from each
12 participant. The T1-weighted MRI images can be treated differently in this pipeline based on the
13 age of the participants and image quality. The segmentation process uses tools from AFNI
14 (Analysis of Functional NeuroImages; <https://afni.nimh.nih.gov>) to generate a label map that can
15 readily be imported into AtlasViewerGUI, a visual graphical user interface contained within
16 Homer2 (<https://homer-fnirs.org/>) (14,19), providing brain and skull surfaces used in the analysis
17 of the fNIRS data (note that AtlasViewerGUI is also available in Homer3). The steps of the
18 segmentation process are outlined here along with the options that can be employed to handle
19 scans from infants as well as low SNR images.

20 The starting point for the processing pipeline is an anatomical T1-weighted image that
21 approximately has the nose aligned with the y-axis of the scanner (i.e., the nose should be pointing
22 forward (anterior) in an axial image). If the orientation of the nose is more than 15 degrees from
23 this orientation -- for example in a sleeping infant -- we have found it helpful to rotate the image

1 such that the nose is roughly aligned with the y-axis for initiating the pipeline. This can be done
2 using 3drotate from AFNI or similar functionality from other image analysis packages. Next, the
3 image is resampled (3dresample) into a standard Right-Axial-Superior orientation. This ensures
4 that the image will be oriented properly once imported into AtlasViewer. The next step of the
5 segmentation pipeline is bias field correction (3dUnifize); this is optional and can be used if large
6 variations in the signal exist across the image. We then create a brain mask to define brain tissue
7 in the image. This step is sensitive to the age of the subject being analyzed since infants have a
8 significantly smaller intracranial volume as compared to adults. Thus, this step has two options to
9 generate the brain mask: 3dSkullstrip and ROBEX (20). The 3dSkullstrip option performs well in
10 most cases and the user is provided with the ability to set the initial radius and expansion rate for
11 the sphere inflation used in the underlying algorithm. In infant scans, we have found improved
12 performance with the ROBEX-based brain mask. For details on using these functions, please see
13 the instruction guide available at [https://github.com/developmentaldynamicslab/MRI-](https://github.com/developmentaldynamicslab/MRI-NIRS_Pipeline)
14 [NIRS Pipeline](https://github.com/developmentaldynamicslab/MRI-NIRS_Pipeline).

15 The next step of the pipeline is to put the T1 weighted scan into AC-PC alignment. To do
16 this, the brain mask in the prior step is used to extract the brain from the T1-weighted image, which
17 is subsequently aligned with a skull-stripped Talairach Atlas image using auto_tlrc command from
18 AFNI. The rigid body transform from the resulting transform is saved and used to reorient the
19 subject T1-weighted scan and brain mask into AC-PC alignment. Next, we pad the image with
20 zeros. This ensures that the surface generated will be ‘closed’ when imported into AtlasViewer.
21 We then generate a skull mask from the image by identifying an optimal threshold (3dClipLevel)
22 for background removal. The resulting mask generated from thresholding at this optimal level is
23 then filled to define all voxels within the skull. The next step of the pipeline is optional and median

1 filters the image. This may be necessary for low SNR images. The final step of the pipeline uses
2 the 3dSeg command from AFNI to define the tissue into gray matter, white matter, and CSF. The
3 resulting segmentation is then combined with the skull segmentation to generate a label map that
4 contains 4 labels: gray matter, white matter, CSF, and skull.

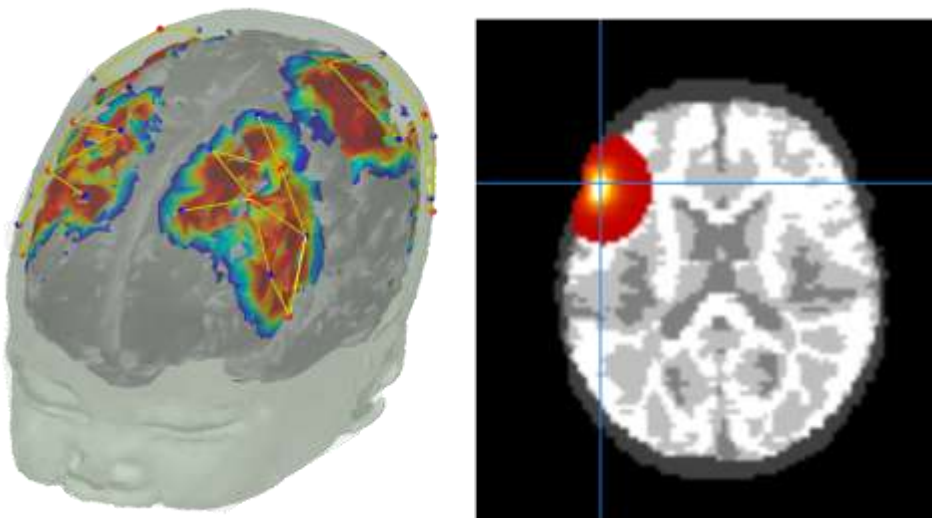
5 Difficulties in this processing pipeline can arise when the original T1-weighted MRI image
6 has a large amount of background noise, such as having captured additional objects (such as the
7 participant's arm) in the scan. For these more extreme cases, we have found it helpful to align the
8 scan to a template, and then create a filled mask of the template, which is used to remove the
9 background noise from the original scan. This leaves the image with only the head and no objects
10 in the background. Further information on this is provided in the pipeline instructions in the
11 repository.

12 Once these steps are complete, the label map can then be read into Homer2/Homer3 to create
13 the anatomical files needed for the spatial prior (i.e., the light model). This image is read in using
14 the import MRI functionality from *AtlasViewerGUI*, and then anatomical reference points are
15 selected by the user. This allows for the construction of the anatomy which can then be combined
16 with the cleaned digitizations from the prior step.

17 **4 Photon Migration Simulation**

18 The next step is to create the light model that will be used for image reconstruction. As this uses
19 previously described tools (14), we describe these steps briefly here. We used the *AtlasViewerGUI*
20 package within Homer2 or Homer3 to project the corrected digitized points for each participant
21 onto the segmented atlas created by cleaning up and segmenting the participant's MRI scan. To
22 ensure that the photon migration simulations were age-specific, absorption and scattering
23 coefficients for the scalp, CSF, gray and white matter for both wavelengths of light were provided

1 such that each node of the mesh was assigned optical properties determined by tissue type based
2 on values from the literature (17,21–24). Photon migration Monte Carlo simulations with 100
3 million photons were run to generate sensitivity profiles for each channel and wavelength. In the
4 data presented here, this process was carried out using the High Performance Computing cluster
5 supported by the Research and Specialist Computing Support service at the University of East
6 Anglia, which enabled the running of simulations for all channels and participants in parallel by
7 utilizing multiple cores. As this is computationally expensive, we recommend use of a server or
8 other high performance computing device for this step. Alternatively, users looking to reduce
9 computation time can reduce the number of simulations down to 10 million or use MCX as
10 implemented through the more recent versions of *AtlasViewerGUI* (9). Next, the head volume and
11 the sensitivity profiles were converted into NIFTI format for use in image reconstruction. Sample
12 photon migration simulations are shown on a segmented head from the MRI scan of a 6-month-
13 old infant in Figure 5a. The head volume and an exemplar channel for the same participant is
14 shown in Figure 5b.



15

1 *Figure 5.* (a) Photon migration simulations on a segmented head of an MRI scan from a 6-month-
2 old infant. (b) Sensitivity profile of an exemplar channel from the same participant in NIFTI
3 format (visualized using *Mango*)

4 **5 Pre-processing fNIRS data in channel-space**

5 For the purposes of demonstrating the quality of image reconstruction below, we used data from a
6 TechEn CW7 system (12 sources and 24 detectors) with wavelengths of 690 nm and 830 nm. Fiber
7 optic cables were used to carry data from the machine to a customized probe geometry of 40
8 channels covering bilateral frontal and parietal cortices (see Figure 5a). fNIRS data in the examples
9 provided here were pre-processed using the *EasyNIRS* package in Homer2. In the pipeline
10 documentation on github, we also provide guidance for users of Homer3 and the snirf file format.
11 Raw data was pruned to include channels with signals between 80 dB and 130 dB using the
12 *enPruneChannels* function which prunes channels based on the signal to noise ratio. Next, these
13 data were converted to optical density units using the *hmrIntensity2OD* function. Motion artifacts
14 were corrected using the *hmrMotionCorrectPCArecuse* function which used targeted principal
15 components analysis (25) [tMotion = 1.0, tMask = 1.0, StdevThresh = 50 and AmpThresh = 0.5].
16 The corrected data was examined for uncorrected motion artifacts using
17 *hmrMotionArtifactByChannel* [tMotion = 1.0, tMask = 1.0, StdevThresh = 50 and AmpThresh =
18 0.5]. If these uncorrected artifacts fell within -1 to 18 seconds of a stimulus trigger, that trigger
19 was removed from further data processing using the *enStimRejection* function. Finally, these data
20 were bandpass filtered using the *hmrBandpassFilt* function with high-pass and low-pass cutoff
21 frequencies of 0.016 and 0.5 Hz, respectively. Relevant information from these processed .nirs
22 files were then used in subsequent steps.

1 **6 Image Reconstruction and Verification**

2 The next step in the processing pipeline is image reconstruction. This step integrates the 3D light
3 model created using *AtlasViewer* with the channel-based fNIRS data processed using Homer2 or
4 Homer3. The image reconstruction is conducted in Matlab using NeuroDOT tools (17)
5 (https://github.com/WUSTL-ORL/NeuroDOT_Beta). In the sections below, we provide an
6 overview of the image reconstruction approach including details for streamlining processing steps
7 between *AtlasViewer*, Homer2/Homer3, and NeuroDOT. We then show sample image-
8 reconstructed data plotted relative to the channel-based fNIRS data.

9 *6.1 Overview of Image Reconstruction in NeuroDOT*

10 First, the sensitivity volumes for each source-detector pair that were calculated in *AtlasViewer*
11 were converted into NeuroDOT format. In NeuroDOT, the sensitivity volumes are arranged in a
12 single two-dimensional matrix A with measurements in the first dimension and voxels in the
13 second dimension. A structure variable *info* contains sub-structures that house meta-data
14 describing the sensitivity volumes (*info.tissue*), the optode locations (*info.optodes*), the
15 measurement list (*info.pairs*), the stimulus paradigm (*info.paradigm*), and other parameters from
16 data acquisition (*info.system*). The header that contains the spatial meta-data from the NIFTI *.nii
17 files from *AtlasViewer* is contained within *info.tissue.infoT1*. The order of the measurements in A
18 corresponds to that described in the measurement list located in *info.pairs*. The voxels are ordered
19 as if the entire sensitivity volume is unwrapped into a single vector. To maximize computational
20 efficiency, only voxels with a sensitivity above a given threshold for any of the measurements are
21 included. The indexing of these voxels relative to the entire volume is described in the variable
22 *info.tissue.dim.Good_Vox*. This step typically saves around a factor of 5-10x in disk space and
23 lowers computation time due to lower demand on RAM. For this study, the threshold was set to

1 0.01 of the maximum sensitivity within the combined volumes of all measurement sensitivity
2 profiles.

3 Second, the preprocessed optical density data from Homer2 in the *.nirs file (or *.snirf file
4 in the case of Homer3) was converted directly into NeuroDOT format. The NeuroDOT
5 measurement list represented in the table *info.pairs* is populated from the *SD* variables in Homer2
6 (or *snirfdata.data.measurementList* in Homer3). The table *info.pairs* contains the source, detector,
7 wavelength, source-detector separation in 2- and 3-dimensions, and other information for each
8 measurement. The measurements to be used for reconstruction are listed in the *info.MEAS.GI*
9 variable. The stimulus paradigm timing information is populated into *info.paradigm* for use in the
10 post-reconstruction analyses (described below).

11 To minimize contributions from extra-cerebral tissue in the variance of the measurement
12 data, we performed global signal regression separately for each wavelength. The mean signal
13 across all low-noise measurement channels was regressed from all channels in a manner akin to
14 superficial signal regression as previously described using the NeuroDOT function *regcorr* (26–
15 28). Though short measurement channels were not utilized in these data, the mean across all
16 measurement channels provides an estimate of systemic physiology present in all of the data.
17 Removing this global mean increases the contrast to noise and spatial specificity of the variance
18 remaining in the measurement data. The conversion of measurement-wise data to voxel-wise data
19 through reconstruction significantly increases the overall size of the optical data due to the
20 presence of many times more voxels than measurements. To help alleviate the large computational
21 demands, the data was temporally down-sampled to 25 Hz before reconstruction using the
22 NeuroDOT function *resample_tts*.

1 Once the optical, sensitivity, and meta-data have been converted into NeuroDOT format, the
2 sensitivity matrix can be inverted separately for each wavelength using the Moore-Penrose
3 generalized inverse with a Tikhonov regularization parameter of $\lambda_1=0.01$ and spatially variant
4 regularization parameter of $\lambda_2=0.1$ using the NeuroDOT function *Tikhonov_invert_Amat* (29). The
5 Tikhonov regularization parameter tunes the balance between spatial smoothness and high-spatial
6 frequency noise in the image. Spatially variant regularization helps control for the tendency for
7 DOT methods to reconstruct too superficially and is set to optimize spatial correspondence with
8 fMRI based on other studies (30). This process minimizes the objective function:

9 $\min\{\|y_{meas} - Ax\|_2^2 + \lambda_1 \|Lx\|_2^2\}$. We include λ_2 as a spatially variant regularization term, such that:

10 $\text{diag}(L) = \sqrt{[\text{diag}(A^T A) + \lambda_2]}$ (26,30,31). Given these regularization steps, the direct inverse that

11 provides the solution, $x = A_{\lambda_1, \lambda_2}^\# y_{meas}$ is given by the Moore-Penrose generalized inverse:

12 $A_{\lambda_1, \lambda_2}^\# = L^{-1}(A^T \tilde{A} + \lambda_1 I)^{-1} A^T y_{meas}$ with $\tilde{A} = \tilde{A} L^{-1}$. Regularization parameters of $\lambda_1=0.01$ and $\lambda_2=0.1$

13 work well for a broad range of geometries and array designs. These steps are all carried out within
14 *Tikhonov_invert_Amat.m*. We also recommend using at least a modest amount of direct spatial
15 smoothing using a Gaussian smoothing kernel to control for speckly noise in the images.
16 Recommended smoothing kernel sizes range from 3-10 mm at their full width at half max. The
17 optical data are reconstructed into the voxelated space using the NeuroDOT function
18 *reconstruct_img*.

19 Relative changes in oxygenated (HbO₂), deoxygenated (HbR), and total hemoglobin (HbT)
20 concentrations are obtained from the reconstructed absorption coefficients by spectral
21 decomposition of the extinction coefficients of HbO₂ and HbR at the two wavelengths (32,33).

1 Conversion from relative changes in absorption coefficients to HbO₂ and HbR is performed with
2 the NeuroDOT function *spectroscopy_img*.

3 4 *6.2 Sample Image Reconstructed Data*

5 Figure 6 below shows samples of image reconstructed fNIRS data from one participant plotted
6 against the processed channel-based fNIRS data. To create these images, we first placed the
7 centroid of a 2cm diameter sphere at the maximum value of each channel's sensitivity volume
8 from the photon migration simulations for each chromophore. Note that we constrained the
9 sensitivity volumes to the cortex to ensure that the maximum value was located in the cortex and
10 not in the skull or surface tissues. Next, we extracted the mean reconstructed fNIRS time series
11 from each sphere, averaging over voxels within the sphere. The red curve in each panel shows the
12 mean image-reconstructed time series, while the black line shows the channel-based data from the
13 associated channel. We show data from 6 channels in total (see brain images in Figures 6E, F for
14 mapping of channels to spheres). We selected these channels because they are located in parietal
15 and ventral occipital regions of interest for our sample data set. As can be seen in the figure, the
16 image-reconstructed data match the channel-based data well for both HbO₂ (Figure 6A,B) and
17 HbR (Figure 6C, D) . The signals are within the same range, with the image-reconstructed data
18 typically showing a bit more signal intensity.

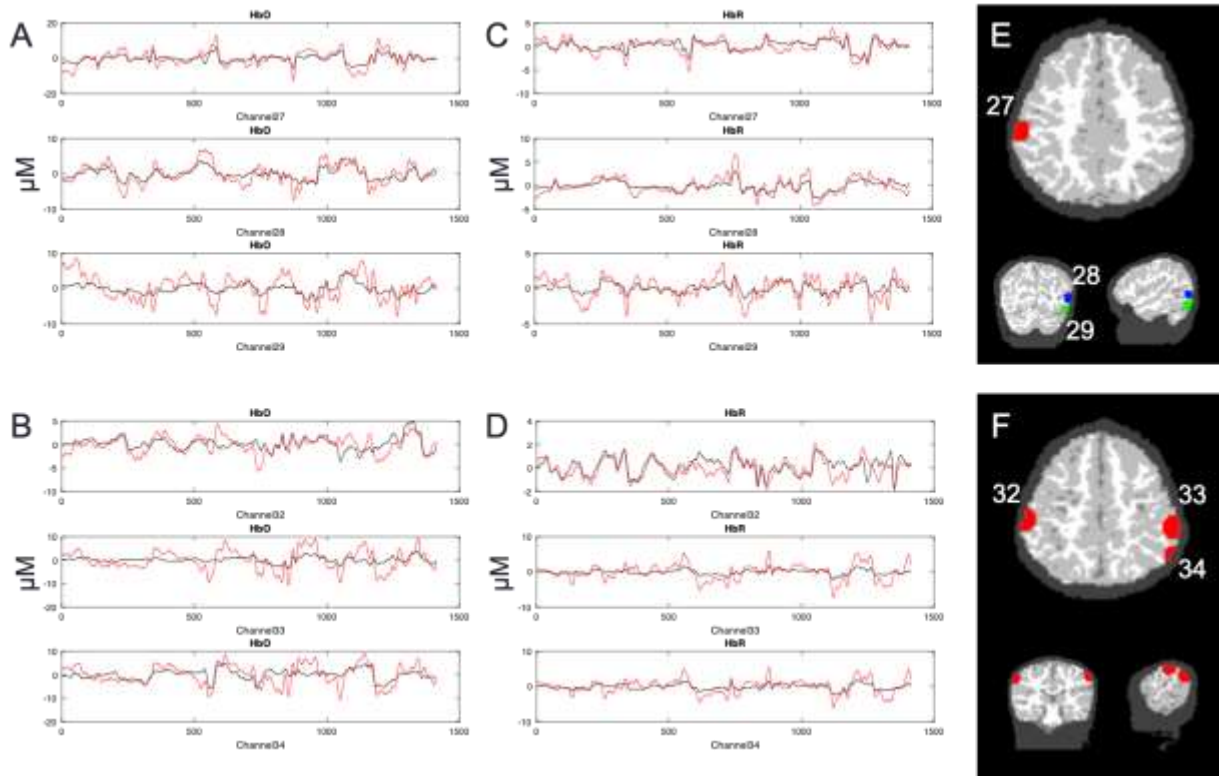
19

20

21

22

23

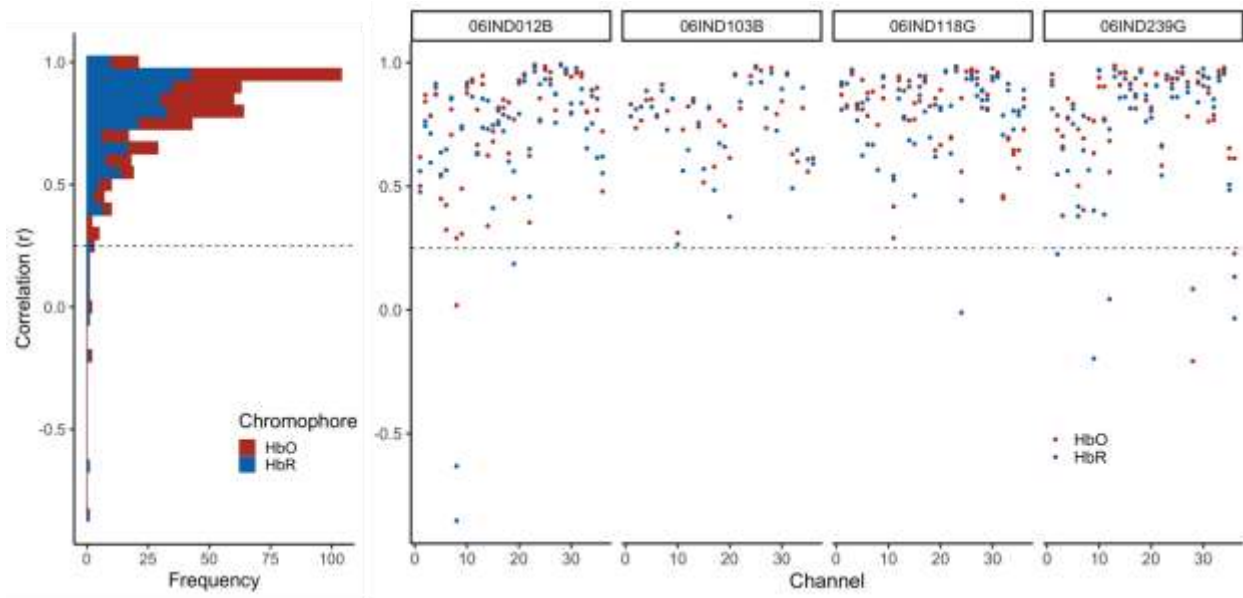


1
 2 *Figure 6.* Image reconstructed fNIRS data (red lines) plotted against channel-based fNIRS data
 3 (black lines). Left panels show HbO time series (in μM) for channels 27-29 (A) and channels 32-
 4 34 (B); middle panels show HbR time series for channels 27-29 (C) and channels 32-34 (D). Panel
 5 E shows the locations of the spheres used to extract data for channels 27-29. Note that different
 6 colors are used to show the channels across views in E as the axial slice does not match the coronal
 7 and sagittal views. Panel F shows the locations of the spheres associated with channels 32-34
 8 (axial, coronal, and sagittal views are all aligned).

9 *6.3 Verifying the Image Reconstruction Approach*

10 To verify the image reconstruction approach, we correlated the average image-reconstructed
 11 time series (e.g., red lines in Figure 6) with the channel-based time series (e.g., black lines in Figure
 12 6) for all data runs for four sample participants. In total, we conducted 504 correlations: 7 runs
 13 (over 4 participants) x 36 channels x 2 chromophores (HbO₂/HbR). Data from 18 channels were

1 discarded because the channels were pruned in the initial fNIRS processing. The correlation results
2 are shown in Figure 7. Most of the correlations were quite high and above our minimum acceptable
3 threshold of 0.25. In particular, 473 of 496 correlations were greater than 0.25; the mean r value
4 for this subset was 0.8. Thus, only 2.6% of the sample was below the criterion. In these cases, the
5 channel-based fNIRS data was of low quality with poor SNR.



6
7 *Figure 7.* Verifying the fNIRS image reconstruction data. Each dot shows the correlation between
8 the image-reconstructed fNIRS data averaged over a 2cm sphere in cortex (see examples in Figure
9 6E,F) and the associated channel-based data. Red dots show correlations for HbO; blue dots show
10 correlations for HbR. Data are shown for four participants (see columns). Three participants
11 (06IND012B, 06IND118G, 06IND239G) had multiple runs, so there are four correlation values
12 per channel (HbO/HbR for run1 and run2). Dashed line shows our target criterion value of 0.25.
13 The vast majority of comparisons were above the criterion value.

1 **7 Individual-level Analysis of Data (General Linear Model)**

2 Once the participant fNIRS data have been reconstructed, a typical approach is to model these
3 time series data using general linear modelling. For our test dataset, brain responses were
4 analyzed using a general linear model (GLM) run with the NeuroDOT function *GLM_181206*.
5 We used a hemodynamic response function (HRF) derived from DOT data as it has been shown
6 to be a better fit for optical data than those derived from fMRI (34). The same HRF was used for
7 HbO₂ and HbR responses. Each event was modelled with a 10 second extent and variable inter-
8 trial intervals with an exponentially distributed set of durations. We focused our analyses over
9 the window from one second before each stimulus onset to 20 seconds post onset. To control for
10 variability in the number of events per run and per participant, we computed a weighted average
11 of the betas over runs, weighted by the number of events per condition in each run. The functions
12 included in the pipeline allow the user to use the default NeuroDOT HRF as we did here;
13 alternatively, the user can specify a custom HRF file to use.

14 **8 Transfer to Group Space and Group-level Analysis**

15 This step employs a common or group space for the study. Often it is convenient to use the MNI
16 coordinate system to report functional activation since it is the standard space used for fMRI and
17 PET activation studies. The registration from subject space to the atlas space is driven by the
18 AC-PC aligned image and brain mask generated in Section 3 and corresponding T1-weighted
19 image and brain mask of the template image for the group space. We used ANTS software to
20 implement a hierarchical image registration procedure that includes a high dimensional
21 diffeomorphic non-linear symmetric image normalization (35) as the last step in the registration.
22 The prior steps of the image registration hierarchy include a rigid body registration followed by

1 an affine registration. The resulting transform was then applied to the HbO₂ and HbR beta maps
2 from the individual-level GLM results.

3 **9 Demonstration of the pipeline on an example dataset from NIRSSport (NIRX)**

4 To demonstrate the type of data the processing pipeline yields, we report sample results here
5 from a second test dataset taken using a NIRSSport (NIRx) system. This has the added utility of
6 showing that our pipeline generalizes across NIRS systems (as the prior examples in this report
7 used a TechEn system). The data presented in this case study are part of a longitudinal study
8 investigating the effects of schooling on neurocognitive function (36).

9 *Participants.* Data from seventy-four 4.5-year-old children (34 females, M age = 53.5
10 months, $SD = 1.3$) who participated in a longitudinal study in Scotland were used to verify the
11 analyses pipeline. The study was conducted in the participants' homes. Parents gave written
12 informed consent and children gave verbal assent prior to the testing session. The research was
13 approved by the General University Ethics Panel (GUEP 375) at the University of Stirling.

14 *Experimental Task.* Visual working memory (VWM) performance was measured as
15 children took part in a color change detection task (37). The experimenter explained the task to
16 the children using 3x3 inch flash cards. Once the experimenter was satisfied that the children
17 understood the rules, they moved to the experiment. The experimental task was run in E-prime
18 V.3 software on an HP laptop with a 14-inch screen. In each trial, a fixation appeared on either
19 side of the screen to orient the child to the screen. Then, a memory array of colored squares was
20 presented for 2 seconds, followed by a blank screen for 1 second (delay period). Then, a test
21 array of colored squares was presented and stayed on the screen until a response was made. After
22 the presentation of the test array, the child was asked whether the colored squares were 'same' or
23 different' between the memory and test arrays. The experimenter registered the child's response

1 using the keyboard. Each trial was followed by an inter-trial interval of 1 second (50% of the
2 trials), 3 seconds (25% of the trials), or 5 seconds (25% of the trials). VWM load was
3 manipulated from 1 to 3 items (load 1, load 2 and load 3). There were 8 trials for the same
4 condition and 8 trials for the different condition for each load. Thus, there were 12 possible
5 conditions for trials in this task, 3 loads (1, 2 and 3) x 2 trial types (same and different) x
6 accuracy (correct and incorrect).

7 *fNIRS Data Acquisition.* A NIRSport system (NIRX) with 8 sources and 8 detectors was
8 used to collect neuroimaging data from children as they engaged in the VWM task. Data were
9 collected at 7.81 Hz and the wavelengths of the sources was 760 nm and 850 nm. Probe
10 geometry with fourteen channels overlaying the bilateral frontal and parietal areas (see Figure
11 8a) was constructed based on regions of interest from previous fMRI VWM literature (38). The
12 head circumference of the child was measured and a suitable cap was chosen. Four cap sizes
13 were used across all children and source-detector distances were scaled according to cap size (50
14 cm: 2.5 cm, 52 cm: 2.6 cm, 54 cm: 2.7 cm and 56 cm: 2.8 cm). The distances from the nasion to
15 inion and between the peri-auricular points were measured to ensure that the cap was centrally
16 placed on the child's head.

17 *fNIRS Data processing.* The probe geometry was digitized to obtain the coordinates of
18 sources and detectors for each of the four capsizes. A 4.5-year-old MRI atlas was obtained from
19 the Neurodevelopmental MRI database (39–43) and segmented into four tissue types (scalp,
20 CSF, grey matter and white matter). Monte Carlo simulations were run with 1 million photons to
21 generate sensitivity profiles for channels for each capsize (step 2, see Figure 1). The head
22 volume and sensitivity profiles were converted into NIFTI format. Next, channel-based fNIRS
23 raw data was pre-processed, corrected for motion artifacts, filtered, and converted to optical

1 density units. Data were also corrected for superficial scalp artifacts using global signal
2 regression (step 3). These channel-based fNIRS optical density data was integrated with the
3 volumetric sensitivity profiles using image reconstruction as described previously (step 4).

4 A general linear model with 6 regressors (for 12 conditions) was run on each voxel by
5 convolving a modified gamma function from SPM (delay of response = 4; delay of undershoot =
6 15, dispersion of response = 1; dispersion of undershoot = 1; ratio of response to undershoot = 6;
7 onset =0; length of kernel =16) (44) with a boxcar window of duration 4.5 seconds (step 5). Note
8 that this gamma function was chosen after visually comparing the duration of response onset,
9 time to peak and response offset of the generated HRFs and conventional channel-based block
10 averages. Further, this boxcar window was chosen to account for a sample array of 2 seconds,
11 delay of 1 second and the rest of the time dedicated towards the test array period. Beta
12 coefficient maps were obtained for all 12 conditions in each voxel for each chromophore and
13 participant. Next, these individual-level beta maps were registered to the MNI space (step 6). For
14 Group analyses, the beta maps were entered into a linear mixed effects model (using *3dLME*
15 function in AFNI) with within-subjects factors of load, trial type, and chromophore (HbO and
16 HbR). Note that only correct trials were used for our analyses. For the current case-study, we
17 focused on the interaction between load and chromophore to examine whether HbO activation in
18 significant clusters show the canonical trend of increasing activation with increasing VWM load.
19 Only those voxels that contained data from 60% of the subjects were included for further
20 analyses. To control the family-wise error in our data, we used the *3dFWHMx* function in AFNI
21 to estimate the empirical ACF in our fNIRS data and fit a mixed ACF model to this function. We
22 then used the mixed-ACF parameters (0.9939 8.3354 5.2485) in *3dClustSim* with a voxelwise p

1 = 0.01, alpha = 0.05, and 10,000 iterations. We selected two-sided thresholding with the NN1
2 option (first-nearest neighbour clustering). The cluster size criterion was 169 voxels.

3 *Results.* Two clusters showed a significant interaction between load and chromophore: left
4 middle frontal gyrus and left angular gyrus. Figure 8b shows the two clusters in red. Block
5 averaged change in HbO/HbR activation extracted from these clusters are also shown. In the left
6 angular gyrus, HbO activation increased with increasing load. In the left middle frontal gyrus,
7 activation was highest for load 2. Activation in both regions show the canonical difference
8 between HbO and HbR activation, with the largest difference visible at the higher loads. Masked
9 sensitivity profiles from channels 5, 6, 7 and 8 in the left frontal cortex and 12, 13 and 14 in the
10 left parietal cortex are shown in yellow. Block-averaged activation from these channels are
11 shown in Figure 8c. We see similar trends in activation with increasing load between the block
12 averages from the significant clusters from the image reconstruction approach and block
13 averages from the conventional channel-based approach. Image reconstruction provides more
14 precise localization of the source of activation in the brain. The change in activation with
15 increasing load is more pronounced when localized to the left angular gyrus compared to the
16 changes in activation in the three channels. It is important to note that the goal of employing
17 image reconstruction techniques is not to empirically compare against and arrive at the same
18 result observed in channel space. Instead, it affords the opportunity to obtain spatial localization
19 of activation from multiple channels to specific clusters and compare these activation maps
20 across participant groups and ages while accounting for key sources of spatial variance in the
21 data.

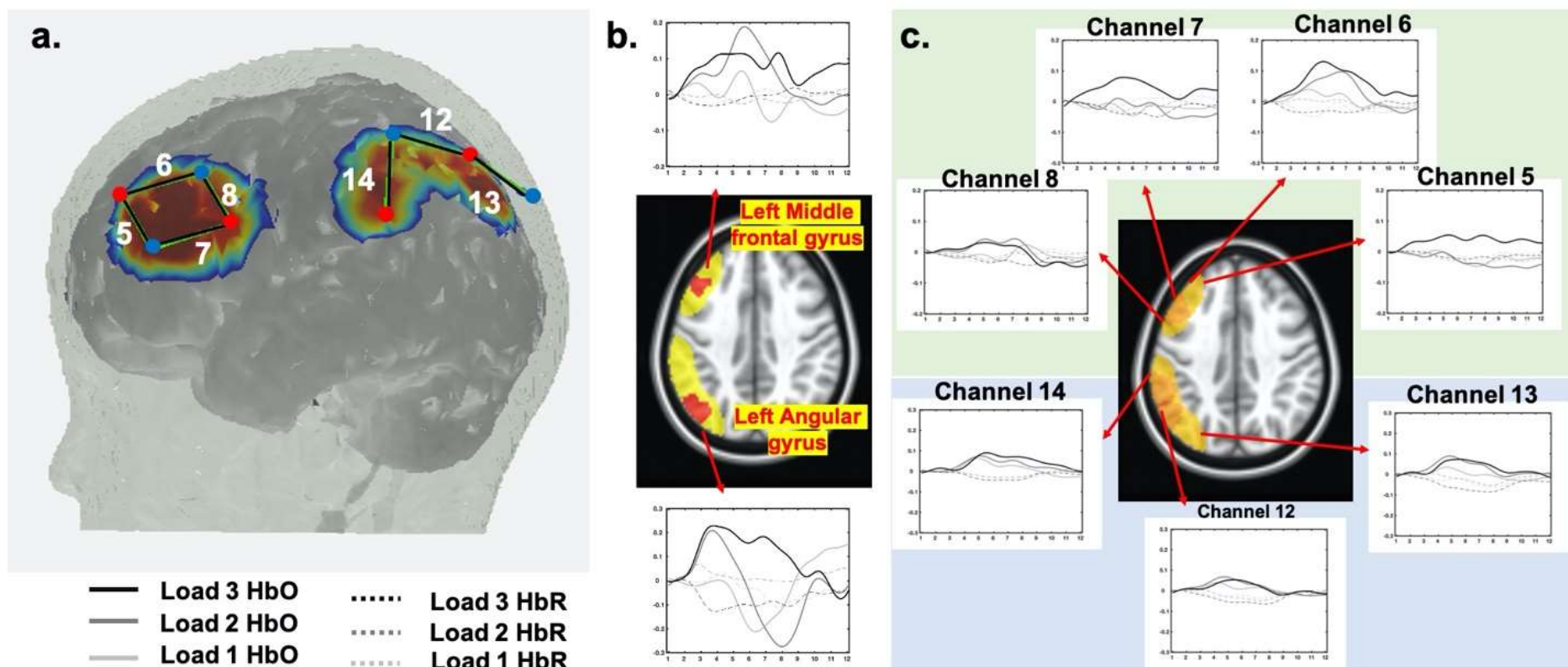


Figure 8. a. Probe geometry for the task. b. Significant clusters from the image-reconstructed fNIRS data in the middle frontal gyrus and left angular gyrus (see red clusters in brain image). Time series plots show weighted average HbO₂ (solid lines) and HbR (dashed lines) for load 1 (light grey), load 2 (medium grey), and load 3 (black) conditions. c. Block-averaged activation from the channel-based fNIRS data showing channels overlapping with the red clusters in (b) (see highlighted yellow region in brain image). Plotting conventions as in (b).

1 **10 Discussion/Conclusion**

2 Image reconstruction of fNIRS data is a critical tool in standardizing the spatial location of fNIRS
3 data from both individual and multiple channels into voxel space. Doing so allows for analysis of
4 fNIRS data based on anatomical region rather than channel, accounting for several known sources
5 of spatial variance in the data including variance in exact optode location on any given participant.
6 This approach also enables users to tap powerful fMRI analysis tools in the process. Despite the
7 considerable benefits of this approach, there are complexities in the analysis that make image
8 reconstruction difficult. These include a lack of standard approaches for cleaning digitized optode
9 locations and creating templates, standardizing individual anatomies, creating a light model based
10 on either template or individual data, running the general linear model, moving the data into a
11 common space, and analyzing the data. In the present article, we described a flexible pipeline with
12 accompanying code to push through these complexities along with initial verification data acquired
13 from different fNIRS systems.

14 In the present report, we demonstrated that with fNIRS data and both individual anatomical
15 MRI images and templates, fNIRS data can be reconstructed in a manner that correlates with the
16 original channel-based data, and is analyzable in voxel space. The accompanying publicly
17 available code can be adapted by users for their own data requirements. The code also contains
18 additional functionality not discussed in the current paper, such as functions to cross-check GLM
19 results against the time-course data from a given region. We also demonstrated with datasets from
20 child fNIRS studies that the analyses and reconstruction methods are reliable and correspond with
21 the measurements taken in channel space.

22 There are important limitations in the reconstruction of fNIRS data to consider. The methods
23 and data we describe show a high level of correspondence between the reconstructed data and the

1 channel-based data; however, it would be useful in future to work to validate the pipeline using
2 synthetic data. It would also be useful for future work to clarify how different sources of variability
3 contribute to reconstruction accuracy, evaluating, for instance, the relative contributions of the
4 optical properties used during photon migration versus mis-localization in optode position
5 estimates. We also note that our pipeline is not fully automated; rather, users must make key
6 decisions at different points. We have highlighted several decision points in this paper. Additional
7 discussion is provided in the on-line documentation. We stress that users should verify their data
8 as they move through the pipeline to understand what effect these decisions have on the data and
9 to make sure, for instance, that the sensitivity profile created after photon migration simulations
10 matches the locations of optodes. Finally, we note that the photon migration method we used works
11 best with a high-performance computing cluster. To reduce this overhead, we recommend the use
12 of MCX (9).

13 The pipeline presented here contains several important contributions to the field. In the
14 *digitizeR* package for the R language, we present a novel method of creating digitization templates
15 and preparing them for use with other software. In addition, we provide code, suggestions and
16 guidelines for the cleaning and segmenting of individual MRIs to turn individual anatomical data
17 into a brain model suitable for use in the creation of a light model. We then used a combination of
18 existing software to demonstrate how to create a light model, perform a general linear model, and
19 move data into group space for analysis. While some individual aspects of this pipeline, such as
20 the creation of a light model, feature in a number of software packages, these have not previously
21 been combined in a way that allows users to go from raw data to final group analyses as reported
22 here. The pipeline reported here, therefore, provides a roadmap of the functionality that users
23 require to take their data all the way through analysis. As such, we hope this paper will be of use

1 to software developers and others interested in creating standardization of analysis approaches
2 within a rapidly developing field.

3

4 **Disclosures.** The authors have no competing interests to disclose.

5 **Acknowledgements.** This work supported by Grant No. OPP1164153 from the Bill & Melinda
6 Gates Foundation and Grant No. R01HD083287 from the National Institutes of Health. Both grants
7 were awarded to J. P. Spencer. The authors are grateful for the contributions of Aaron Buss and
8 Jessica Defenderfer for their comments during testing of the pipeline. We also thank [Meryem](#)
9 [Yücel](#) and Stephen Tucker for their help making the pipeline compatible with Homer3 and the
10 .snirf format.

11

12

13 **Data, code, and materials availability.** The code required to run the analyses is available at
14 https://github.com/developmentaldynamicslab/MRI-NIRS_Pipeline. The code for digitizeR is
15 available at <https://github.com/samhforbes/digitizeR>. Data used in this manuscript can be made
16 available upon request to the authors.

17

18 **Bibliography**

- 19 1. Custo A, Boas DA, Tsuzuki D, Dan I, Mesquita R, Fischl B, et al. Anatomical atlas-guided
20 diffuse optical tomography of brain activation. *NeuroImage*. 2010 Jan;49(1):561–7.
- 21 2. Kim HY, Seo K, Jeon HJ, Lee U, Lee H. Application of Functional Near-Infrared
22 Spectroscopy to the Study of Brain Function in Humans and Animal Models. *Molecules and*
23 *Cells*. 2017 Aug 31;40(8):523–32.
- 24 3. Curtin A, Tong S, Sun J, Wang J, Onaral B, Ayaz H. A Systematic Review of Integrated
25 Functional Near-Infrared Spectroscopy (fNIRS) and Transcranial Magnetic Stimulation
26 (TMS) Studies. *Front Neurosci*. 2019 Feb 28;13:84.

- 1 4. Delgado Reyes L, Wijekumar S, Magnotta VA, Forbes SH, Spencer JP. The functional
2 brain networks that underlie visual working memory in the first two years of life.
3 *NeuroImage*. 2020 Oct;219:116971.
- 4 5. Walsh B, Tian F, Tourville JA, Yücel MA, Kuczek T, Bostian AJ. Hemodynamics of speech
5 production: An fNIRS investigation of children who stutter. *Sci Rep*. 2017 Dec;7(1):4034.
- 6 6. Lloyd-Fox S, Blasi A, McCann S, Rozhko M, Katus L, Mason L, et al. Habituation and
7 novelty detection fNIRS brain responses in 5- and 8-month-old infants: The Gambia and UK.
8 2019;17.
- 9 7. Wijekumar S, Kumar A, M. Delgado Reyes L, Tiwari M, Spencer JP. Early adversity in
10 rural India impacts the brain networks underlying visual working memory. *Dev Sci*. 2019
11 Mar 21;e12822.
- 12 8. Fishell AK, Arbalaez AM, Valdes CP, Burns-Yokum TM, Sherafati A, Richter EJ, et al.
13 Portable, field-based neuroimaging using high-density diffuse optical tomography. 2020;12.
- 14 9. Fang Q, Boas DA. Monte Carlo Simulation of Photon Migration in 3D Turbid Media
15 Accelerated by Graphics Processing Units. *Opt Express*. 2009 Oct 26;17(22):20178.
- 16 10. Doulgerakis-Kontoudis M, Eggebrecht A, Wojtkiewicz S, Culver J, Dehghani H. Toward
17 real-time diffuse optical tomography: accelerating light propagation modeling employing
18 parallel computing on GPU and CPU. *J Biomed Opt*. 2017 Dec 1;22(12):1.
- 19 11. Tian F, Kozel FA, Yennu A, Croarkin PE, McClintock SM, Mapes KS, et al. Test-retest
20 assessment of cortical activation induced by repetitive transcranial magnetic stimulation with
21 brain atlas-guided optical topography. *J Biomed Opt*. 2012 Nov 7;17(11):116020.
- 22 12. Cooper RJ, Caffini M, Dubb J, Fang Q, Custo A, Tsuzuki D, et al. Validating atlas-guided
23 DOT: A comparison of diffuse optical tomography informed by atlas and subject-specific
24 anatomies. *NeuroImage*. 2012 Sep;62(3):1999–2006.
- 25 13. Ferradal SL, Eggebrecht AT, Hassanpour M, Snyder AZ, Culver JP. Atlas-based head
26 modeling and spatial normalization for high-density diffuse optical tomography: In vivo
27 validation against fMRI. *NeuroImage*. 2014 Jan;85:117–26.
- 28 14. Aasted CM, Yücel MA, Cooper RJ, Dubb J, Tsuzuki D, Becerra L, et al. Anatomical
29 guidance for functional near-infrared spectroscopy: AtlasViewer tutorial. *Neurophoton*. 2015
30 May 5;2(2):020801.
- 31 15. Zhan Y, Eggebrecht AT, Culver JP, Dehghani H. Image Quality Analysis of High-Density
32 Diffuse Optical Tomography Incorporating a Subject-Specific Head Model. *Front*
33 *Neuroenerg* [Internet]. 2012 [cited 2021 Jan 4];4. Available from:
34 <http://journal.frontiersin.org/article/10.3389/fnene.2012.00006/abstract>

- 1 16. Huppert TJ, Diamond SG, Franceschini MA, Boas DA. HomER: a review of time-series
2 analysis methods for near-infrared spectroscopy of the brain. *Appl Opt.* 2009 Apr
3 1;48(10):D280.
- 4 17. Eggebrecht AT, Culver JP. NeuroDOT: An extensible Matlab toolbox for streamlined optical
5 functional mapping. In: *Clinical and Preclinical Optical Diagnostics II* [Internet]. Munich:
6 Optical Society of America; 2019. p. 11074_26. (SPIE Proceedings; vol. EB101). Available
7 from: http://www.osapublishing.org/abstract.cfm?URI=ECBO-2019-11074_26
- 8 18. Kabsch W. A solution for the best rotation to relate two sets of vectors. *Acta*
9 *Crystallographica Section A.* 1976 Sep 1;32(5):922–3.
- 10 19. Tsuzuki D, Cai D, Dan H, Kyutoku Y, Fujita A, Watanabe E, et al. Stable and convenient
11 spatial registration of stand-alone NIRS data through anchor-based probabilistic registration.
12 *Neuroscience Research.* 2012 Feb;72(2):163–71.
- 13 20. Iglesias JE, Cheng-Yi Liu, Thompson PM, Zhuowen Tu. Robust Brain Extraction Across
14 Datasets and Comparison With Publicly Available Methods. *IEEE Trans Med Imaging.* 2011
15 Sep;30(9):1617–34.
- 16 21. Eggebrecht AT, White BR, Ferradal SL, Chen C, Zhan Y, Snyder AZ, et al. A quantitative
17 spatial comparison of high-density diffuse optical tomography and fMRI cortical mapping.
18 *NeuroImage.* 2012 Jul;61(4):1120–8.
- 19 22. Bevilacqua F, Pigué D, Marquet P, Gross JD, Tromberg BJ, Depeursinge C. In vivo local
20 determination of tissue optical properties: applications to human brain. *Appl Opt.* 1999 Aug
21 1;38(22):4939.
- 22 23. Custo A, Wells III WM, Barnett AH, Hillman EMC, Boas DA. Effective scattering
23 coefficient of the cerebral spinal fluid in adult head models for diffuse optical imaging. *Appl*
24 *Opt.* 2006 Jul 1;45(19):4747–55.
- 25 24. Strangman G, Franceschini MA, Boas DA. Factors affecting the accuracy of near-infrared
26 spectroscopy concentration calculations for focal changes in oxygenation parameters.
27 *NeuroImage.* 2003 Apr;18(4):865–79.
- 28 25. Yücel MA, Selb J, Cooper RJ, Boas DA. Targeted principle component analysis: A new
29 motion artifact correction approach for near-infrared spectroscopy. *J Innov Opt Health Sci.*
30 2014 Mar;07(02):1350066.
- 31 26. Zeff BW, White BR, Dehghani H, Schlaggar BL, Culver JP. Retinotopic mapping of adult
32 human visual cortex with high-density diffuse optical tomography. *Proceedings of the*
33 *National Academy of Sciences.* 2007 Jul 17;104(29):12169–74.
- 34 27. Gregg. Brain specificity of diffuse optical imaging: improvements from superficial signal
35 regression and tomography. *Front Neuroenerg* [Internet]. 2010 [cited 2021 Jan 4]; Available
36 from: <http://journal.frontiersin.org/article/10.3389/fnene.2010.00014/abstract>

- 1 28. Saager RB, Telleri NL, Berger AJ. Two-detector Corrected Near Infrared Spectroscopy (C-
2 NIRS) detects hemodynamic activation responses more robustly than single-detector NIRS.
3 NeuroImage. 2011 Apr;55(4):1679–85.
- 4 29. Eggebrecht AT, Ferradal SL, Robichaux-Viehoever A, Hassanpour MS, Dehghani H, Snyder
5 AZ, et al. Mapping distributed brain function and networks with diffuse optical tomography.
6 Nature Photonics. 2014 Jun 1;8(6):448–54.
- 7 30. Wheelock MD, Culver JP, Eggebrecht AT. High-density diffuse optical tomography for
8 imaging human brain function. Review of Scientific Instruments. 2019 May;90(5):051101.
- 9 31. Culver JP, Durduran T, Furuya D, Cheung C, Greenberg JH, Yodh AG. Diffuse Optical
10 Tomography of Cerebral Blood Flow, Oxygenation, and Metabolism in Rat during Focal
11 Ischemia. J Cereb Blood Flow Metab. 2003 Aug;23(8):911–24.
- 12 32. Bluestone AY, Abdoulaev G, Schmitz CH, Barbour RL, Hielscher AH. Three-dimensional
13 optical tomography of hemodynamics in the human head. Opt Express. 2001 Sep
14 10;9(6):272.
- 15 33. Prah, Scott. Tabulated Molar Extinction Coefficient for Hemoglobin in Water [Internet].
16 1998. Available from: <https://omlc.org/spectra/hemoglobin/summary.html>
- 17 34. Hassanpour MS, White BR, Eggebrecht AT, Ferradal SL, Snyder AZ, Culver JP. Statistical
18 analysis of high density diffuse optical tomography. NeuroImage. 2014 Jan;85:104–16.
- 19 35. Avants B, Epstein C, Grossman M, Gee J. Symmetric diffeomorphic image registration with
20 cross-correlation: Evaluating automated labeling of elderly and neurodegenerative brain.
21 Medical Image Analysis. 2008 Feb;12(1):26–41.
- 22 36. McKay C, Shing YL, Rafetseder E, Wijekumar S. Home assessment of visual working
23 memory in pre-schoolers reveals associations between behaviour, brain activation and
24 environmental measures. Developmental Science. In Press;
- 25 37. Simmering VR. The development of visual working memory capacity during early
26 childhood. Journal of Experimental Child Psychology. 2012 Apr;111(4):695–707.
- 27 38. Wijekumar S, Spencer JP, Bohache K, Boas DA, Magnotta VA. Validating a new
28 methodology for optical probe design and image registration in fNIRS studies. NeuroImage.
29 2015 Feb;106:86–100.
- 30 39. Evans AC. The NIH MRI study of normal brain development. NeuroImage. 2006
31 Mar;30(1):184–202.
- 32 40. Sanchez CE, Richards JE, Almli CR. Age-specific MRI brain templates for healthy brain
33 development from 4 to 24 years. 2010.
- 34 41. Sanchez CE, Richards JE, Almli CR. Age-Specific MRI Templates for Pediatric
35 Neuroimaging. Developmental Neuropsychology. 2012 Jul;37(5):379–99.

1 42. Richards JE, Xie W. Brains for All the Ages. In: Advances in Child Development and
2 Behavior [Internet]. Elsevier; 2015 [cited 2021 Jan 4]. p. 1–52. Available from:
3 <https://linkinghub.elsevier.com/retrieve/pii/S0065240714000299>

4 43. Richards JE, Sanchez C, Phillips-Meek M, Xie W. A database of age-appropriate average
5 MRI templates. NeuroImage. 2016 Jan;124:1254–9.

6 44. Penny W, Friston KJ, Ashburner J, Kiebel S, Nichols T. Statistical Parametric Mapping: The
7 Analysis of Functional Brain Images. 1st Edition. 2006.

8